

# Printed, metallic thermoelectric generators integrated with pipe insulation for powering wireless sensors

Brian Iezzi<sup>a</sup>, Krishnamraju Ankireddy<sup>b</sup>, Jack Twiddy<sup>a</sup>, Mark D. Losego<sup>c</sup>, Jesse S. Jur<sup>a,\*</sup>

<sup>a</sup> Department of Textile Engineering, Chemistry, and Science, North Carolina State University, Raleigh, NC 27606, United States

<sup>b</sup> Conn Center for Renewable Energy Research, University of Louisville, Louisville, KY 40292, United States

<sup>c</sup> School of Materials Science and Engineering, Georgia Institute of Technology, Atlanta, GA 30332, United States

## HIGHLIGHTS

- Flexible thermoelectric generators are screen printed with low cost metallic inks.
- Thermoelectric generators are integrated into radial pipe insulation.
- 15 cm section of pipe insulation is used to power a wireless sensing circuit.
- Electrical configuration of thermoelectric device is optimized for a D.C. to D.C. converter.

## ARTICLE INFO

### Keywords:

Thermoelectric generator  
Screen printing  
Internet of things  
Pipe insulation  
Wireless sensing network

## ABSTRACT

The Internet of Things (IoT), coupled with advanced analytics, is poised to revolutionize manufacturing maintenance and efficiency. However, a practical route to powering these many IoT devices remains unclear. In this work, flexible thermoelectric generators (TEGs) are fabricated from low cost, screen printed silver and nickel inks before being integrated into a novel form factor device based on commercial steam pipe insulation. Through optimization of internal resistances and total device design, this 420-junction TEG device produces 308  $\mu$ W of power at a temperature difference of 127 K. This is sufficient to power a temperature sensing circuit with wireless communication capabilities. In this report we demonstrate that, after an initial 4 h of charging, this TEG can power a standard RFduino microcontroller for 10 min while sending temperature readings every 30 s via Bluetooth Low Energy (BLE) to a cell phone. Additional optimization and scaling could further increase system efficiency and provide a viable route to powering an industrial wireless sensing network (WSN).

## 1. Introduction

The Internet of Things (IoT) has the capability to transform industrial manufacturing. Pervasive IoT monitoring of vibrations, stresses, corrosion, and thermal fluctuations will provide critical data for better maintenance prediction and scheduling. However, the labor costs associated with battery replacement in IoT devices is impractical, necessitating cost effective, continuous power sources to support this form of ubiquitous sensing. Here, we seek to use abundant waste heat streams available in most industrial settings as the source for this power.

More than 50% of the energy consumption in the United States results in waste heat [1]. Low-grade waste heat (less than 230 °C) is particularly underutilized because typical recovery methods (such as a heat exchanger) are less economically viable at low temperatures.

However, this lower quality heat is available in such large quantities (950 trillion kJ per year) that the work potential of this stream is 35% higher than medium grade (230–650 °C) and 110% higher than high grade (> 650 °C) sources [2]. Consequently, modestly efficient, low-grade heat recovery may be the ideal solution to powering low-power industrial IoT sensors.

Currently, the most viable route to harnessing this wasted heat is through the use of thermoelectric generators (TEGs). In recent years, the theoretical limits of these generators have been continually pushed by advances in nanotechnology and have made new application areas, such as wireless sensing, more viable [3–6]. The sheer number of sensors and, consequently, power sources that would be required for these networks has driven a specific focus on creating simple and scalable manufacturing processes for TEGs. Large area printing of TEGs has quickly emerged as a promising path forward [7–8]. The current

\* Corresponding author at: 1020 Main Campus Drive, Raleigh, NC 27606, United States.  
E-mail address: [jsjur@ncsu.edu](mailto:jsjur@ncsu.edu) (J.S. Jur).

<http://dx.doi.org/10.1016/j.apenergy.2017.09.073>

Received 24 May 2017; Received in revised form 31 August 2017; Accepted 11 September 2017  
0306-2619/ © 2017 Published by Elsevier Ltd.

benchmarks for high efficiency thermoelectric conversion rely on toxic and relatively rare metals such as bismuth (Bi), lead (Pb), tellurium (Te), and antimony (Sb). While these have been used widely to produce printed modules [9–11] cost and environmental concerns remain as barriers to large scale implementation in industry. When considering the cost (economically and environmentally) of a potential thermoelectric, the base material cost and the cost of production are the main driving forces. Printed thermoelectrics are capable of simultaneously addressing both concerns due to the wide variety of deposition techniques (screen printing, inkjet printing, molding, lithography, vacuum deposition) and inorganic/organic material combinations possible (carbon nanotubes, semiconducting polymers, metal powders) [12].

A significant amount of prior work has been carried out on the development of high aspect ratio and high power density flexible printed TEGs for use in wearable applications [13–15] and in industrial facilities [16–18]. Lu et al. used silk fabric as a substrate for solution based bismuth telluride (BiTe) TEG elements. The final device, composed of 12 thermocouples, exhibited 12 nW of power output at temperature differences possible on the body (5–35 K) [15]. Furthermore, Suarez et al. have shown the capabilities of non-solution based bismuth and telluride elements in a flexible matrix [19]. The wearable devices created showed no increase in resistance after 1000 bending cycles to a radius of 5 mm, thus demonstrating the potential durability of flexible devices. Integration of a printed, flexible BiTe TEG with a voltage boost converter has also been demonstrated for use in wearable applications. Veri et al. have shown that a 140 thermocouple device can generate enough voltage to power up a D.C. to D.C. boost converter, similar to that reported later in this work [20].

As wearable devices have addressed increasing interest in health monitoring the same has been true for devices designed with industry system monitoring in mind. Chen et al. have demonstrated combining a curved steam pipe attachment and a commercial TEG to power a wireless sensor [18] while Jovanovic et al. have designed a flexible bismuth telluride device that would meet the power requirements of a sensing network [21]. More recently, Madan et al. applied a printed, flexible BiTe TEG to an insulated heat pipe. A high power density of  $2.8 \text{ W m}^{-2}$  was reported while utilizing forced convection to maintain a temperature gradient [22]. The concept demonstrated in that work shows that the common piping found in many industrial facilities has great potential for further development. It is important to note that, for both the wearable and industrial spaces, the vast majority of the literature work relies on bismuth, antimony, and tellurium due to high efficiencies. Capabilities of other, less toxic thermoelectric elements has been investigated to a lesser extent and utilizing a flexible, printed TEG to power an industrial wireless sensing network has not yet been demonstrated.

In this work, we introduce several new accomplishments: (1) screen printing of a 420 junction TEG module based solely upon relatively inexpensive and non-toxic materials, and (2) utilizing this TEG to power a wireless sensing system in a realistic industrial scenario. Inspiration for a novel device matrix was drawn from standard steam pipe insulation found in facilities worldwide. Single planar modules were embedded in insulation radially, thus creating a harvesting device that takes advantage of waste heat in all directions. A visualization of this setup can be seen in Fig. 1. One six inch (15 cm) section of insulation is demonstrated to power a microcontroller, temperature probe, and wireless transmission relay for 10 min of continuous data transmission at 30 s intervals after a 4 h charging period.

## 2. Experimental procedure

### 2.1. Device fabrication and evaluation

The TEGs in this work were printed from commercial silver (Ag) ink and in-house formulated nickel (Ni) pastes [23]. Silver paste was DuPont 5064 H (discontinued, now 5065). Nickel paste was prepared from

1–5  $\mu\text{m}$  nickel flakes (Atlantic Equipment Engineers, Upper Saddle River, NJ.) The flakes were suspended in ethylene glycol with polyvinylpyrrolidone (PVP, molecular weight 40,000 g/mol) as the binding agent. The total solids content of the final paste was 82% with a PVP fraction of 2%. The silver served as the p-type Seebeck material while nickel was the n-type. The structures were screen printed on 125  $\mu\text{m}$  thick polyimide (Kapton®) films. All of the printed TEG legs were 20 mm long with each Ag element being 2 mm in width and each Ni element being 3.5 mm in width. Silver was printed via one pass through the screen (approximately 20  $\mu\text{m}$  thick after sintering) while the nickel was printed in two passes (approximately 90  $\mu\text{m}$  thick after sintering). Conductivity was achieved in the silver samples via oven curing at 120 °C for 30 min while the nickel required sintering at 350 °C under an inert argon atmosphere for 3 h. Ink characterization was previously reported [23]. Each module consisted of 35 junctions with the electrical leads being attached via silver epoxy (Chemtronics CW2400). Leads were low resistance copper-clad steel yarns sourced from Bekaert Corporation. Samples were encapsulated using Polyonics XT-621 polyimide film.

A simulated heat pipe was constructed from a 3.5 in. outer diameter carbon-steel pipe. A 1.5 kW rigid heating element was inserted into the pipe and regulated with a PID controller to within 2 °C of the set point temperature (usually 300 °C). One inch thick fiberglass insulation (Carolina Plumbing Supply) was cut lengthwise to insert the thermoelectric modules and the paper/aluminum foil cover that originally covered the insulation was replaced after insertion of the modules. Images of a single TEG power module, TEG insertion into the insulation, and complete device can be seen in Fig. 1. It is also important to note that all testing reported was conducted with the previously mentioned thermally insulating cover on the outside of the overall device. This is significant because it prevents an effective heat sink from being created with the air, reducing the temperature differential from 160 °C to 130 °C. This reduction in temperature differential hurts device efficiency but is a more realistic use-case scenario. All testing was completed without the use of any heat sinking material or forced convection from outside sources such as a fan. Thermal imaging was conducted using a FLIR Thermal Camera to demonstrate this point and supporting images can be found in Fig. S1 in the supplementary materials [24–30]. TEG power modules were electrically connected in various series and parallel configurations. Optimization of these configurations is discussed later. The temperature gradient was assessed by taking the temperature reported by an Omega Engineering J type thermocouple attached to the PID controller (hot side) and subtracting the reading from another thermocouple attached to the “cold side” of a thermoelectric element. Thermal and electrical data was collected using a Keithley 2750 multimeter. Voltage output is measured at the end of the connected leads allowing for current, internal resistance, and power output to be derived using a matched load potentiometer.

### 2.2. Circuit design

The circuit used to collect and transmit data consisted of four main elements: a D.C. to D.C. boost converter, a microcontroller, a temperature sensor, and a receiver. A circuit diagram along with a flow chart of the various elements and actual bread-boarded circuit can be seen in Fig. 2. The boost converter was a Linear Technologies LTC3108 that had previously been integrated onto a breakout made by Crispytronics. This breakout included a coupled inductor with a 1:100 turns ratio, allowing the LTC3108 to be powered up on input voltages of as little as 20 mV. Both a standard electrolytic capacitor and an electric double-layer capacitor (EDLC, more commonly referred to as a supercapacitor) were used in this study. A 2.2 mF, 35 V Nichicon aluminum electrolytic capacitor (from here referred to as  $C_{OUT}$ ) was placed between the  $V_{OUT}$  pin of the D.C. to D.C. converter and the ground while a 100 mF 5 V PowerStor supercapacitor (from here referred to as  $C_{STORE}$ ) was placed between the  $V_{STORE}$  pin and the ground. This supercapacitor

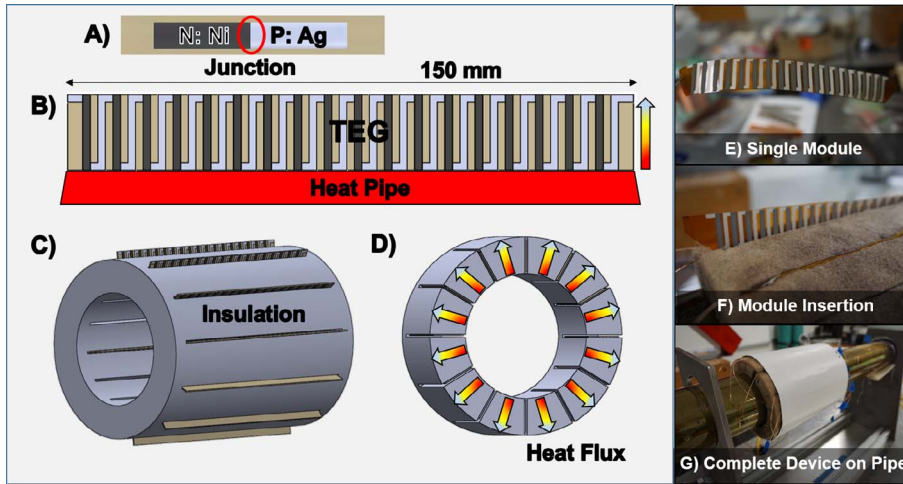


Fig. 1. (A) One junction composed of n-type nickel (Ni) and p-type silver (Ag) inks, (B) Printed thermoelectric module consisting of 35 Ag/Ni junctions with each Ag element being 2 mm in width and each Ni element being 3.5 mm in width, (C) Insertion of 12 modules into steam pipe insulation to create 420 junction device, (D) Cross section view of radial heat transfer through insulation, (E–G) Images of a flexible 35 junction module inserted into the insulation with a cover in place.

has a maximum energy storage potential of 1.25 J if charged to 5 V. When minimum voltage requirements were met, the boost converter powers on, first charging the  $V_{OUT}$  capacitor to the preset voltage (in this case 3.3 V) and then switching to  $V_{STORE}$ . These capacitors are then used to power a microcontroller unit (MCU). The LTC3108 is designed to first drain the energy source on  $V_{OUT}$  (in this case the 2.2 mF capacitor) before switching to the energy source on  $V_{STORE}$  (in this case the 100 mF supercapacitor). An RFduino RFD22102 DIP microcontroller is selected because of its built-in Bluetooth low energy (BLE) communications and analog to digital (ADC) signal conversion. This microcontroller has an ultralow power (ULP) current draw of 4  $\mu$ A, transmit and receive current draw of 12 mA, and output standard drive current

draw of 0.5 mA. The RFduino needs a nominal voltage supply of 3.0 V with a minimum listed at 2.1 V (but found to retain some function down to 1.9 V). An ADC pin included on the RFduino DIP was used with an Analog Devices TMP 36 temperature probe to generate temperature readings. The TMP 36 probe has an average current draw of 50  $\mu$ A. The transmission was received on a Bluetooth enabled phone using the open source RFduino Test application.

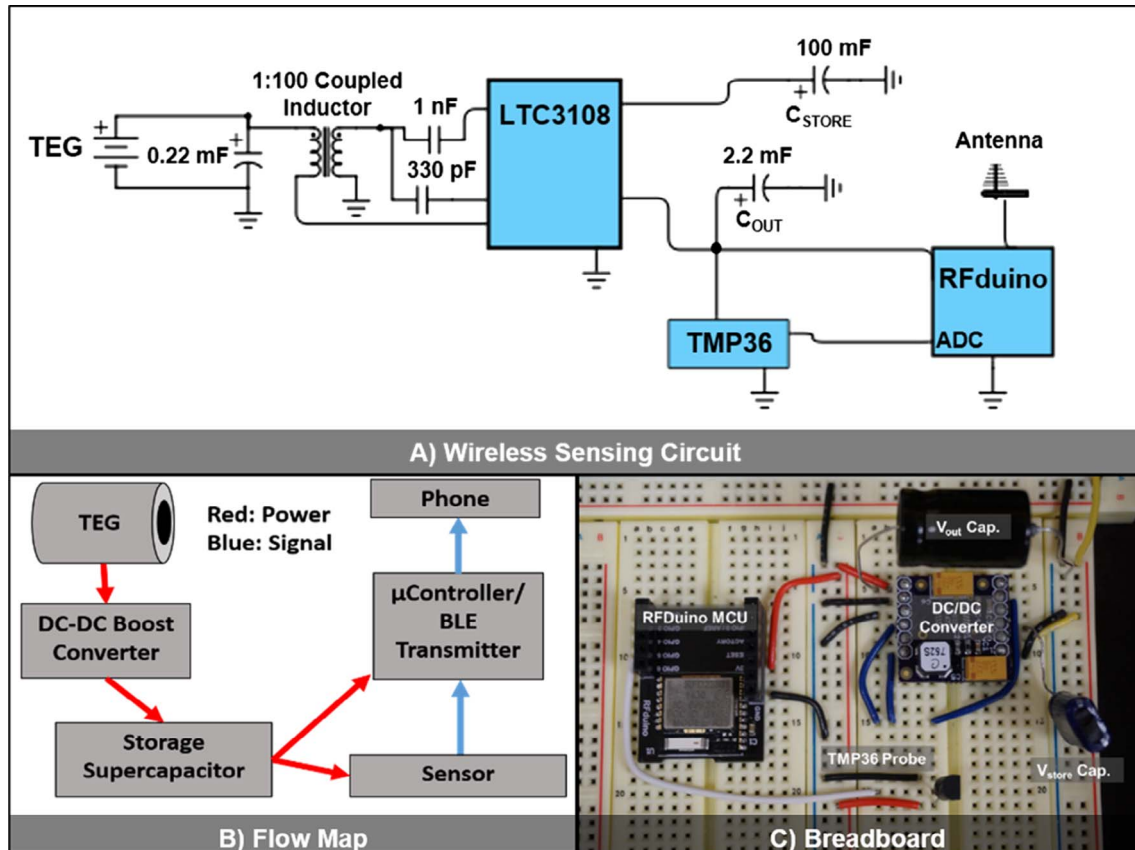
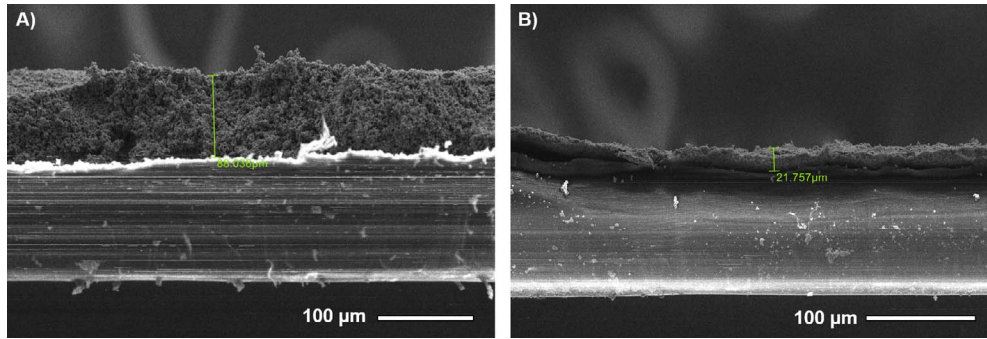


Fig. 2. (A) Wireless sensing circuit with TEG, LTC3108 and Transformer (D.C. D.C. Converter), Storage Capacitors, TMP36 Temperature Probe, and RFduino microcontroller (MCU). (B) Flow map of power and signal through circuit. (C) Breadboard of Fig. 2A.

**Table 1**  
Resistance matching optimization between printed Ag and Ni legs in the TEG module.

	Ink	Resistivity ( $\Omega \text{ m}^{-1}$ )	Width (mm)	Thickness ( $\mu\text{m}$ )	Resistance/Element ( $\Omega$ )	Mismatch ( $\Omega_{\text{Ni}}/\Omega_{\text{Ag}}$ )
Previous	Ag	$4.55 \times 10^{-7}$	5	18	0.10	7.9
	Ni	$1.06 \times 10^{-5}$	5	53	0.80	
New	Ag	$4.55 \times 10^{-7}$	2	22	0.21	3.3
	Ni	$1.06 \times 10^{-5}$	3.5	88	0.69	



**Fig. 3.** (A) Screen printed Ni film with a thickness of 88 microns. (B) Screen printed Ag film with a thickness of 22  $\mu\text{m}$ .

### 3. Results and discussion

#### 3.1. Single module improvement and performance

Besides connecting multiple TEG modules into a monolithic device, we also demonstrate improvement upon our previously reported single TEG module design [23] in two important ways: (1) the electrical resistances between the two printed TE legs are better matched, and (2) each module is encapsulated to improve long term durability of our final TEG system.

Power output of a TEG is driven by module resistance. High resistances decrease power output and mismatched leg resistances can further lower performance [31]. To optimize the latter, printed line widths and film thicknesses are adjusted appropriately. Results of these changes can be seen in Table 1. The printed silver elements are reduced from 5 mm to 2 mm in width while thickness remains roughly constant at 20  $\mu\text{m}$ . The nickel elements are reduced from 5 mm to 3.5 mm in width and increased in thickness from approximately 50  $\mu\text{m}$  to 90  $\mu\text{m}$ . Trace length is held constant at 20 mm. The increase in nickel film thickness is verified with scanning electron microscopy (SEM) in Fig. 3. These changes have two main effects: silver leg resistance increases due

to less cross sectional area, and nickel leg resistance decreases due to a larger cross sectional area. Previously, the nickel legs had a resistance approximately eight times higher than that of the silver. This was reduced to three times difference, leading to better internal matching of leg resistances. Average electrical resistances per junction, calculated by measuring the resistance of an entire module and then dividing by the number of junctions, ranged from 0.1 to 0.2  $\Omega/\text{jcn}$  (Table S1 Supplementary).

In prior work, we also observed these metallic-based TEG modules

increased in electrical resistance by > 40% after a single thermal cycle to 300  $^{\circ}\text{C}$ , presumably due to oxidation [23]. To improve durability, a polyimide encapsulant with silicone adhesive is applied to the modules. For the purposes of a comparison study, eight modules are fabricated with four encapsulated modules and four modules without encapsulation. Fig. 4A plots the average electrical resistances of these modules during two heating cycles from room temperature to 300  $^{\circ}\text{C}$  (the expected use temperature). Modules with a polyimide protective coating show only a 13% increase in electrical resistance, while unprotected modules rise by ~40% in electrical resistance. Additional testing is conducted to evaluate if the increase in resistance after one cycle for the encapsulated samples was typical under further high temperature cycling. Fig. 4B shows the change in resistance for three encapsulated modules over a series of thermal cycles to 300  $^{\circ}\text{C}$ . Most modules show an average increase of 5–10% increase per cycle with one module showing less than 1% increase per cycle. These results are a significant improvement over the previously reported modules without encapsulation and are a critical step towards demonstrating long-term durability.

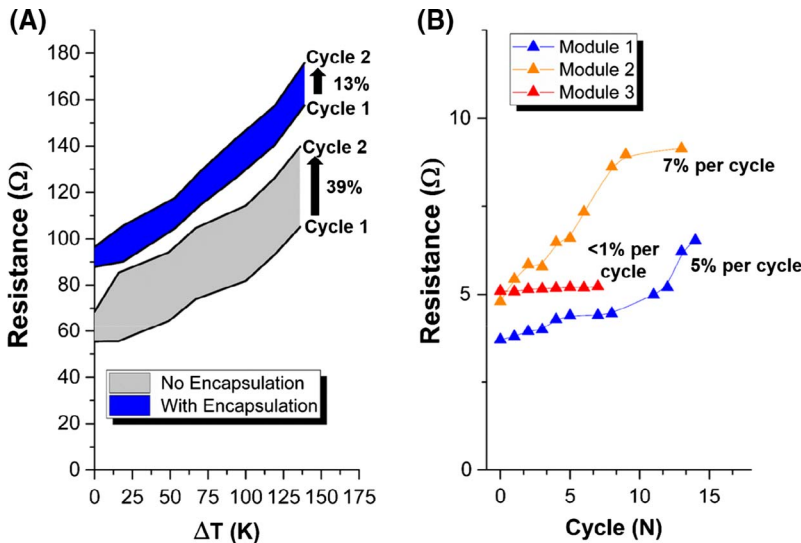


**Fig. 4.** (A) Resistance increase after one thermal cycle for TEG modules with and without encapsulation and (B) Increase in resistance for encapsulated TEG modules over up to 14 thermal cycles with the average increase being approximately 4% per cycle across all modules.



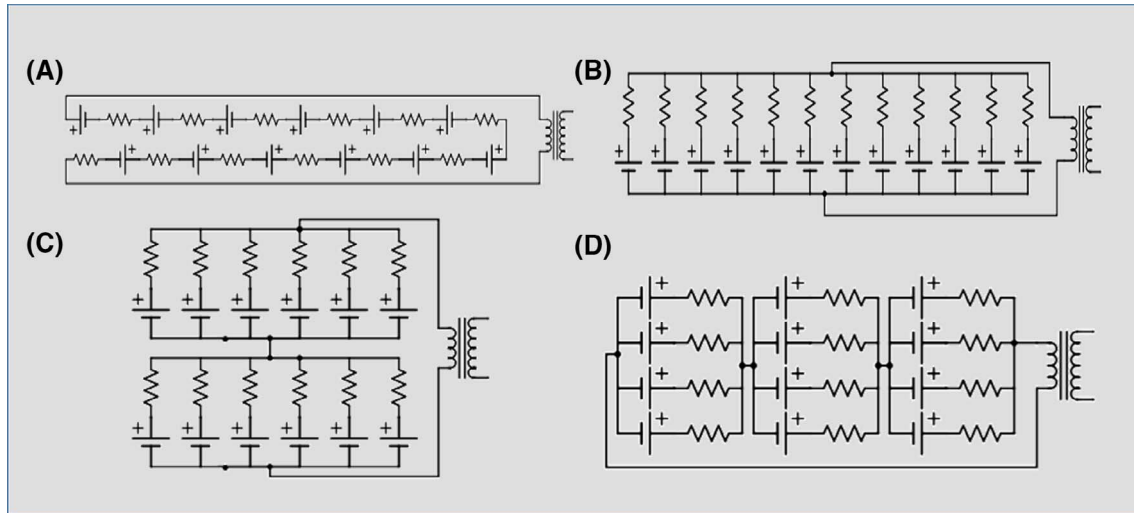


Fig. 5. All tested 12 module device designs with (A) purely series (B) purely parallel (C) A 2 series set of 6 modules in parallel (D) A 3 series set of 4 modules in parallel.

### 3.2. Electrical configuration of complete TEG device

A single TEG module can be electrically modeled as a voltage source in series with an internal resistance. The internal resistance is the summation of the electrical resistances of each TE element (leg). Because screen-printed metallic TEGs have many TE elements the internal resistance of a device can be quite high and must be managed by placing TEG modules in series and parallel combinations as necessitated by the load needing power.

In this case, the load is a D.C. to D.C. boost converter. For our wireless system, a D.C. to D.C. boost converter with a 1:100 turns ratio coupled inductor is selected. This converter enables efficient conversion of low voltages (as small as 20 mV) to the 3.3 V required for our microcontroller. However, the converter requires a power source with an internal resistance of less than 10  $\Omega$  and ideally near 2  $\Omega$  [32]. Achieving a screen-printed TEG device with this level of internal resistance is challenging but possible with a combination of series and parallel module connections. Several of these design combinations are shown in Fig. 5. Design A is a TEG device with all twelve modules in series; Design B has all twelve modules in parallel; Design C has two subsystems of six modules in parallel which are then connected in series; and Design D has three subsystems of four modules in parallel which are also connected in series.

We first model the performance of all of these designs by assuming an average junction resistance of 0.2  $\Omega$ /junction (at room temperature) and a 70% increase in module resistance at the operating hot side temperature of 300  $^{\circ}\text{C}$  [23]. Consequently, a 35 junction module has a theoretical “hot” resistance of 12  $\Omega$ . Utilizing the parallel addition of resistances equation ( $1/R_T = 1/R_1 + 1/R_2 + \dots 1/R_n$ ) as well as series addition ( $R_T = R_1 + R_2 + \dots R_n$ ) theoretical values are calculated and are compared to experimental findings in Table 2. These theoretical calculations appear appropriate for most of the system designs, with most errors at less than 10%. As expected, the purely series design (A) has the highest open circuit voltage (non-loaded), but also the highest

total internal resistance. Conversely, Design B (all in parallel) has the lowest open circuit voltage but also the lowest internal resistance. The input power requirements for the boost converter (20 mV/5  $\Omega$ ) fall within these two bounds. It is worth noting that Design B is capable of starting the boost converter while Design A is not. The remaining designs have generated voltages and internal resistances that meet or are near the minimum requirements. To clarify, the input voltages referenced hereafter are at open circuit for a full 420 junction TEG device.

Design C and Design D are investigated first for suitability with the system. Fig. 6A shows the voltage generated by Design C and D versus temperature difference. As expected, Design D, with three parallel subsystems in series, has approximately three times the voltage output of a purely parallel device (Design B). Design C has approximately two times the voltage for the same reason. Fig. 6B demonstrates the power output of both designs versus a varying load resistance. Design C has a maximum power output of 211  $\mu\text{W}$  at a load resistance of 5.4  $\Omega$  while Design D has a maximum power output of 238  $\mu\text{W}$  at 11.3  $\Omega$ . While Design D may appear to be the optimum choice due its higher voltage and higher power output, the need for long-term energy storage necessitates a device matching the maximum efficiency requirements of our boost converter. For the specific boost converter setup in question (1:100 coupled inductor) the maximum efficiency is 40% at an input voltage of 60 mV and a power supply with internal resistance of 2–10  $\Omega$  [32]. Design C meets both of these requirements at the operating temperature while Design D does not.

It is interesting to note that the optimal configuration for a particular situation largely depends on the TEG’s operating temperature. For example, Design D would be more optimal when operating at a temperature difference of 80 K. To further illustrate this point, a 4 series set of 3 modules in parallel would have a resistance of approximately 16  $\Omega$  and output voltage of approximately 130 V at a temperature difference of 130 K (based on the model illustrated in Section 3.2). Similar to Design D, if this new system was operating at a lower temperature difference (for example 50 or 60 K), this configuration would likely be preferable as its potential for voltage output is higher due to having more modules in series. The modular design presented here would make such adjustments fairly straightforward both during the design process and afterward in the field by using an internal feedback loop that would switch electrical configurations based on fluctuations in temperature.

### 3.3. Demonstration of printed TEG device powering a sensor and wireless transmitter

In operation, the power from the TEG device is delivered through

Table 2  
Electrical characteristics of TEG designs A–D.

Design	Calculated resistance at 275 $^{\circ}\text{C}$ ( $\Omega$ )	Observed resistance at 275 $^{\circ}\text{C}$ ( $\Omega$ )	Percent difference (%)	Observed open circuit voltage at 300 $^{\circ}\text{C}$ (mV)
A	140	150	6.9	450
B	1.0	1.4	33	32
C	4.0	4.1	2.5	67
D	8.9	8.8	1.1	102

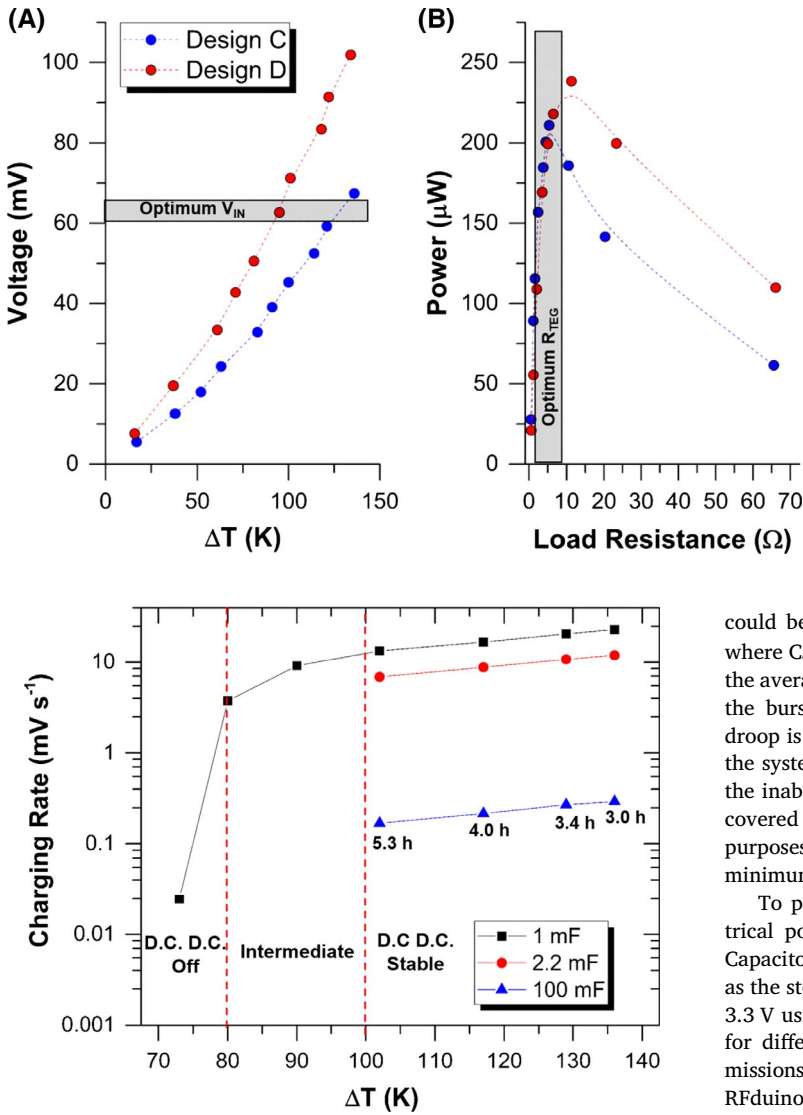


Fig. 7. Charging rate of three storage capacitors versus temperature gradient. The three sections indicate at what temperature the boost converter is able to turn on (with this module configuration), an intermediate phase where it is not consistently charging, and when charging becomes stable. The 100 mF curve shows estimated time to charge to 3.3 V, extrapolated from charging rates measured over a seven minute period.

the boost converter to charge a primary capacitor and a secondary storage supercapacitor. Once charged to 3.3 V, these capacitors deliver the necessary power to start-up the RFduino MCU and temperature sensor. Fig. 7 demonstrates the charging rate of several capacitors at varying TEG operating temperature differentials (as determined by the temperature difference measured at the heat pipe surface and cold side of the module). The minimum requirements for the boost converter are typically first met at a hot side heat pipe temperature of 175 °C (temperature differential of 80 K), although charging rates are slow. Fig. 7 illustrates that charging rates increase with larger temperature differentials but eventually plateau. Further increases in the temperature differential do not significantly increase the charging rate. For use case testing, we use a heat pipe temperature of 300 °C and charge one 2.2 mF capacitor and one 100 mF supercapacitor. This takes approximately 4 h using Design C from Section 3.2.

Choosing the appropriate capacitor depends upon the power requirements of the RFduino microcontroller, including current draw during boot up, advertisement, transmission of a data packet, and ultra-low power (ULP) sleep between transmissions. According to the LTC3108 datasheet, the necessary capacitance for the  $C_{OUT}$  capacitor

Fig. 6. (A) Open circuit voltage of TEG device versus temperature with optimum input voltage for the boost converter indicated and (B) Power output of both designs versus a varying load resistance indicated. Both voltage and resistance were found to be optimum for Design C at the operating temperature difference of 130 K.

could be calculated using the formula  $C_{OUT}(\mu F) = \frac{I_{LOAD}(mA) * t_{PULSE}(ms)}{\Delta V_{OUT}(V)}$  where  $C_{OUT}$  is the capacitance needed for powering the system,  $I_{LOAD}$  is the average current draw of the load in milliamps,  $t_{PULSE}$  is the length of the burst in milliseconds, and  $\Delta V_{OUT}$  is the voltage droop. Voltage droop is the amount of drop-off in voltage possible before brownout of the system. A brownout here is defined as a loss in functionality (e.g., the inability to send transmissions). In practice, this equation was discovered to only be accurate at startup. However, for data-logging purposes, it is essential that the microcontroller remains above its minimum operating voltage to prevent resets of the internal clock.

To properly size the capacitor for continuous operation, the electrical power draw from the microcontroller is empirically assessed. Capacitors for the standard output of the boost converter ( $C_{OUT}$ ) as well as the storage output ( $C_{STORE}$ ) are selected and then charged quickly to 3.3 V using a Keithley 2400. The program on the RFduino is modified for different periods of ultra-low power (ULP) sleep between transmissions of temperature readings drawn from the TMP 36 sensor. The RFduino is then hooked up to the circuit while an external power supply simulates the voltage/current output of Design C (~60 mV) and the amount of time required to drain the capacitors to 1.9 V (resulting in RFduino brownout) is tested. Comparisons between using the RFduino stack ULP delay function as opposed to the standard delay function are made as well. This data is summarized in Table 3.

If the standard delay function is used instead of the ULP delay function, brownouts happen four times faster. Time to brownout is also found to not scale linearly with capacitor size. Despite having more than two orders of magnitude higher capacitance, a 330 mF capacitor's time to brownout with 20 s transmission intervals is only five times longer than a 2.2 mF capacitor. This effect appears to be reasonably independent of transmission interval length as well. Both of these phenomena are believed to be due to the quicker charging times of the smaller capacitor. The continuous power supply of the TEG (even

Table 3  
Characterization of potential storage capacitors.

$C_{OUT}$ (mF)	$C_{STORE}$ (mF)	ULP?	Transmission interval (s)	Time to 1.9 V brownout (s)
330	100	Yes	5	400
330	100	No	5	115
330	100	Yes	20	2780
2.2	100	Yes	20	540
330	100	Yes	300	3260
2.2	100	Yes	300	720

during transmission of signals) means that it is beneficial to have a smaller capacitor that is able to quickly charge and discharge on the primary output of the D.C. to D.C. boost converter. The slow charging time of a much larger capacitor (or supercapacitor in this case) means that once brownout has been reached at 1.9 V it will be slower to recover to the 3.3 V required by the microcontroller. A more effective combination of capacitors is likely possible with a larger  $V_{OUT}$  (primary) capacitor and a potentially smaller  $V_{STORE}$  (secondary) supercapacitor. This would allow for a potentially shorter charging window because the  $V_{STORE}$  charge time is significantly longer.

In regards to supercapacitor selection in general, a supercapacitor was chosen in favor of a secondary (rechargeable) battery or a large standard capacitor for several reasons. A supercapacitor is preferable for the storage role compared to a large standard capacitor due to the large amount of charge storage possible (thousands of Farads) as well as being compatible with our low voltage charging system (supercapacitors are generally rated for less than 5 V). A secondary (rechargeable) battery is possible to use with this system but selection is limited to batteries that are capable of trickle charging and does not include more common lithium ion rechargeable batteries. Supercapacitors also have a longer life span when used in conditions like the consistent charging/discharging cycle that our system requires. A rechargeable battery would need to be replaced on a more frequent basis and thus mitigate some of the autonomous benefit of our proposed sensor network.

Considering that a 2.2 mF capacitor can charge to 3.3 V in under 5 min and the 100 mF capacitor can charge in approximately 4 h, this combination is chosen for initial testing. The successful test of the combination of the radial TEG and the boost circuit is defined as the ability to power the RFduino MCU for at least 10 min while sending temperature readings every 30 s after reaching 3.3 V on both capacitors. After charging for 3.9 h this was achieved with successful data transfer of 20 bytes of data from the included temperature sensor to a paired smart phone. A screen shot of this data transfer can be found in Fig. S4. It is worth noting that this 3.9 h full charge was achieved after the setup had already been at 300 °C for 4 h. This initial 4 h was used to more accurately simulate a realistic scenario in which the TEGs would

be operating (continuous heat being applied over many hours as compared to a “cold” start where long term heat effects are not taken into consideration). Design D was tested as well and found to be significantly slower than Design C with a full charge only being reached after 5 h of continuous heating. At the same temperature difference Design D charges the 100 mF capacitor at approximately  $0.16 \text{ mV s}^{-1}$  compared to  $0.29 \text{ mV s}^{-1}$  for Design C. A charging curve for Design D can be found in Fig. S5 of the supplementary materials. This further supports the original conclusion that Design C has superior transfer efficiency at an operating temperature differential of 130 K. After brownout has been reached the capacitors will begin to recharge but this recharge period will be shorter than the initial charging time. This is because the larger storage supercapacitor is not drained completely to 0 V, only to 1.9 V where brownout occurs.

Throughout this work the 10 min of continuous data transmission reported is based on a 30 s transmission interval. If the interval itself was increased to 10 min, the duration of continuous data transmission would inherently increase due to longer periods of lower current draw in sleep mode. To further develop this point, 20 transmissions are possible in a 10 min window with a 30 s interval. If this interval was increased to 10 min then a broadcast window of 200 min (where the RFduino is up and running) would likely be possible. Theoretically, the current draw of the microcontroller and temperature probe is low enough that an optimum transmission interval (likely on the order of 30 min to 1 h) would allow for continuous transmission over a period of hours without brownout due to the continued power supply of the TEG.

#### 3.4. Comparison to literature reports

A comparison between our system and other screen printed thermoelectric devices reported in the open literature is illustrated in Fig. 8. Most other reports have used high-performance thermoelectric materials like bismuth telluride but other materials, like carbon nanotubes and conductive polymers, were compared as well. Our device compares well with the literature on power output per junction at various temperatures, even outperforming certain BiTe devices. While overall cost per power generated is high for our device due to the silver ink used,

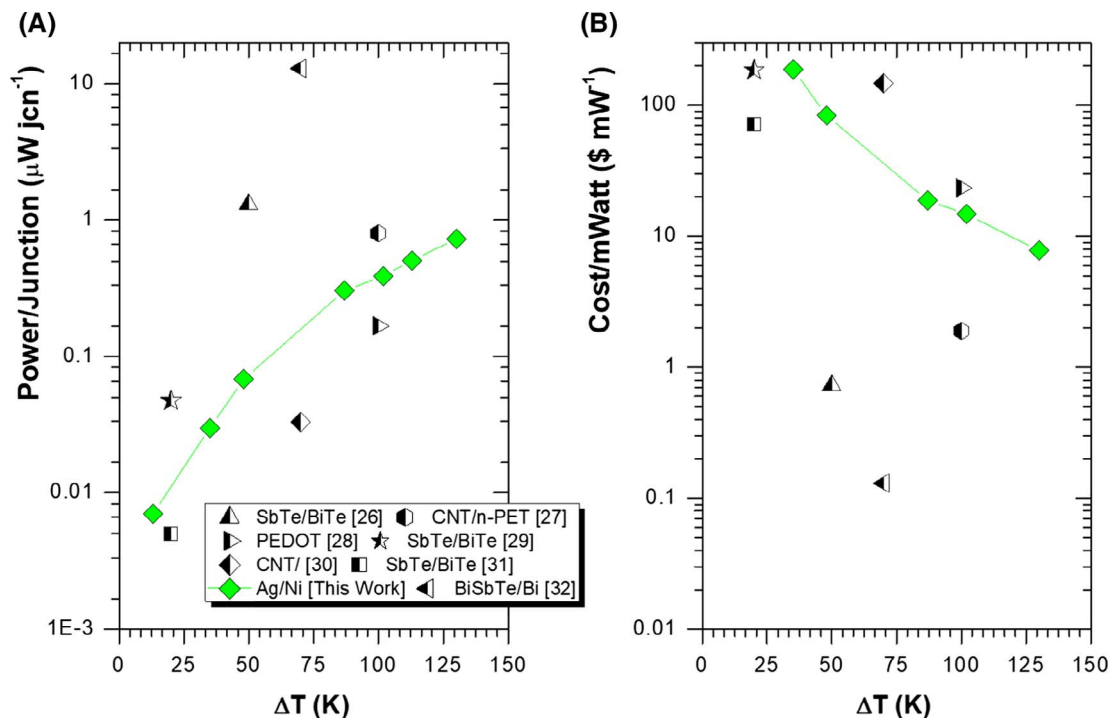


Fig. 8. Comparison of screen printed thermoelectric generators (both organic and inorganic) from literature with the generators demonstrated in this work. (A) Power output per thermocouple and (B) estimated cost per mW of power based on bulk material prices and mass of material used.

the minimal power requirements of cutting edge wireless networks mitigate this drawback. Furthermore, we have also developed a method that is capable of easily producing modules with a large number of elements that have been shown to work at higher temperature differences than other screen printed devices to date. This research has gained enough attention as a potential real world solution for wireless sensing that a test bed has been identified on the NC State University campus to implement these devices in an active monitoring scenario.

#### 4. Conclusions

This paper has realized a radial thermoelectric generator integrated with heat pipe insulation that is capable of powering a sensor circuit with wireless transmission capabilities. Twelve modules comprising a total of 420 thermoelectric junctions were embedded in steam pipe insulation and connected in an optimal configuration to power a D.C. to D.C. boost converter. This boost converter was used to charge a pair of storage capacitors that then turned on a Bluetooth low energy enabled microcontroller. This microcontroller intermittently sent temperature data to a paired nearby phone between ultra-low power sleep states. After applying a protective polyimide coating, thermoelectric modules showed little drop off in power output under hours of continuous use and dozens of thermal cycles, thus demonstrating the potential for long-term stability. Potential areas of further study include optimization of duty cycling of the microcontroller and physical implementation at a realistic test bed on the NC State campus.

#### Acknowledgements

This work was supported by a grant from North Carolina State University, Raleigh, NC, USA through the 2015 Chancellor Innovation Fund. We thank Dr. Philip Bradford and Brian Wells (NC State University) for help in sintering the printed devices and Toby Tung (NC State University) with assistance on scanning electron microscope imaging. K. Ankireddy, M. D. Losego and J. S. Jur have small equity interests in and serve as scientific advisors for Thermo-Flex Technologies, Inc., a company that may potentially benefit from the research results reported herein. The terms of these arrangements have been reviewed and approved by NC State University and the Georgia Institute of Technology in accordance with their conflict of interest policies.

#### Appendix A. Supplementary material

Supplementary data associated with this article can be found, in the online version, at <http://dx.doi.org/10.1016/j.apenergy.2017.09.073>.

#### References

- [1] Lawrence Livermore National Laboratory. U.S. Energy Flow Chart; 2015.
- [2] US Department of Energy. Chapter 6: innovating clean energy technologies in advanced manufacturing - technology assessments. Quarennial Technol Rev 2015.
- [3] Stevens RJ, Weinstein SJ, Koppula KS. Theoretical limits of thermoelectric power generation from exhaust gases. Appl Energy 2014;133:80–8.
- [4] He W, Zhang G, Zhang X, Ji J, Li G, Zhao X. Recent development and application of thermoelectric generator and cooler. Appl Energy 2015;143:1–25.
- [5] Pichanusakorn P, Bandaru P. Nanostructured thermoelectrics. Mater Sci Eng R Reports 2010;67(2–4):19–63.
- [6] Pennelli G. Review of nanostructured devices for thermoelectric applications. Beilstein J Nanotechnol 2014;5(1):1268–84.
- [7] Perelaer J, et al. Printed electronics: the challenges involved in printing devices, interconnects, and contacts based on inorganic materials. J Mater Chem 2010;20:8446–53.
- [8] Khan S, Lorenzelli L. Technologies for printing sensors and electronics over large

flexible substrates: a review. IEEE Sens J 2015;15(6):3164–85.

- [9] Kato K, Hagino H, Miyazaki K. Fabrication of bismuth telluride thermoelectric films containing conductive polymers using a printing method. J Electron Mater 2013;42(7):1313–8.
- [10] We JH, Kim SJ, Kim GS, Cho BJ. Improvement of thermoelectric properties of screen-printed Bi<sub>2</sub>Te<sub>3</sub> thick film by optimization of the annealing process. J Alloys Compd 2013;552:107–10.
- [11] Lee J, Kim HJ, Oh S, Choi SH, Varadan VK. Synthesis and characterization of thermoelectric ink for renewable energy applications; 2012. vol. 8344, p. 83440H-83440H-6.
- [12] Bahk J-H, Fang H, Yazawa K, Shakouri A. Flexible thermoelectric materials and device optimization for wearable energy harvesting. J Mater Chem C 2015;3:10362–74.
- [13] Hyland M, Liu J, Vashae D. Appl Energy Wearable thermoelectric generators for human body heat harvesting; 2016. vol. 182, p. 518–24.
- [14] Deng F, Qiu H, Chen J, Wang L, Wang B. Wearable thermoelectric power generators combined with flexible super capacitor for low-power human diagnosis devices. IEEE Trans Ind Electron 2016;46, p. 1–1.
- [15] Lu Z, Zhang H, Mao C, Li CM. Silk fabric-based wearable thermoelectric generator for energy harvesting from the human body. Appl Energy 2016;164:57–63.
- [16] Gubi E. Thermoelectric-driven autonomous sensors for a biomass power plant; 2013. vol. 42(7). p. 2006–2013.
- [17] Carstens TA, Corradini ML, Blanchard JP, Liu C, Li M, Behdad N. Thermoelectric powered wireless sensors for dry-cask storage; 2013. vol. 60(2). p. 1072–1079.
- [18] Chen J, et al. A thermoelectric energy harvesting system for powering wireless sensors in nuclear power plants; 2016. vol. 63(5). p. 2738–46.
- [19] Suarez F, Parekh DP, Ladd C, Vashae D, Dickey MD, Öztürk MC. Flexible thermoelectric generator using bulk legs and liquid metal interconnects for wearable electronics. Appl Energy 2017;202:736–45.
- [20] Veri C, Francioso L, Pasca M, De Pascali C, Siciliano P, D'Amico S. An 80 mV startup voltage fully electrical DC–DC converter for flexible thermoelectric generators. IEEE Sens J 2016;16(8):2735–45.
- [21] Jovanovic V, Ghamaty S, Bass J. Design, fabrication and testing of a novel energy-harvesting thermoelectric power supply for wireless sensors. PWR2006; 2006. p. 1–9.
- [22] Madan D, Wang Z, Wright PK, Evans JW. Printed flexible thermoelectric generators for use on low levels of waste heat. Appl Energy 2015;156:587–92.
- [23] Ankireddy K, Menon AK, Iezzi B, Yee SK, Losego MD, Jur JS. Electrical conductivity, thermal behavior, and seebeck coefficient of conductive films for printed thermoelectric energy harvesting systems. J Electron Mater 2016;45(11):5561–9.
- [24] Kim SJ, We JH, Cho BJ. A wearable thermoelectric generator fabricated on a glass fabric. Energy Environ Sci 2014;7(6):1959.
- [25] Toshima N, et al. Novel hybrid organic thermoelectric materials: three-component hybrid films consisting of a nanoparticle polymer complex, carbon nanotubes, and vinyl polymer. Adv Mater 2015;27(13):2246–51.
- [26] Wei QS, Mukaida M, Kirihaara K, Naitoh Y, Ishida T. Polymer thermoelectric modules screen-printed on paper. RSC Adv 2014;4(54):28802–6.
- [27] Cao Z, Koukharenko E, Tudor MJ, Torah RN, Beeby SP. Screen printed flexible Bi<sub>2</sub>Te<sub>3</sub>-Sb<sub>2</sub>Te<sub>3</sub> based thermoelectric generator. J Phys: Conf Ser 2013;476:12031.
- [28] Suemori K, Hoshino S, Kamata T. Flexible and lightweight thermoelectric generators composed of carbon nanotube-polystyrene composites printed on film substrate. Appl Phys Lett 2013;103(15).
- [29] Cao Z, Koukharenko E, Torah RN, Tudor J, Beeby SP. Flexible screen printed thick film thermoelectric generator with reduced material resistivity. J Phys: Conf Ser 2014;557(1):12016.
- [30] Madan D, Wang Z, Chen A, Winslow R, Wright PK, Evans JW. Dispenser printed circular thermoelectric devices using Bi and Bi<sub>0.5</sub>Sb<sub>1.5</sub>Te<sub>3</sub>. Appl Phys Lett 2014;104(1):1–5.
- [31] Fang H, et al. Large-scale integration of flexible materials into rolled and corrugated thermoelectric modules. J Appl Polym Sci 2017;134(3).
- [32] Luo J, Boutell M, Brown C. LTC3108 – ultralow voltage step-up converter and power manager. Data Sheet 2010;23(2):1–20.

#### Glossary

*p-type element*: Thermoelectric material where electron holes are the dominant charge carrier

*n-type element*: Thermoelectric material where electrons are the dominant charge carrier

*Junction*: Pair of thermoelectric elements, one p-type and one n-type

*Seebeck coefficient*: Magnitude of potential difference created per unit of temperature difference (typically with units of mV K<sup>-1</sup> or μV K<sup>-1</sup> per junction)

*TEG*: Thermoelectric generator

*Junction*: Connection of one p-type and one n-type element

*Module*: Single 35 junction TEG

*Device*: Connection of twelve 35 junction modules into one 420 junction power supply

*ULP*: Ultra-low power

*DIP*: (Dual in-line package) – rectangular housing with two parallel rows of electrical pins

*BLE*: Bluetooth low energy